Applied Mathematics & Information Sciences
An International Journal

http://dx.doi.org/10.18576/amis/200502

Automated Detection of Diabetic Retinopathy from Fundus Images Using Classical Image Processing

Haitham Issa[1], *Hani Attar*[1], *Jafar Ababneh*[2], *Zakaria Che Muda*[3], *Ismail A. M. Elhaty*[4], *Ahmed Solyman* [5] *and Ramy M. Bahy*[6,*]

[1]Department of Electrical Engineering, Faculty of Engineering, Zarqa University, Zarqa 132222, Jordan
[2]Department of Cyber Security, Faculty of Information Technology, Zarqa University, Zarqa 132222, Jordan
[3]Department of Civil Engineering, Faculty of Engineering and Quantity Surveying, INTI International University, 71800 Nilai, Malaysia
[4]Department of Nutrition and Dietetics, Faculty of Health Sciences, Istanbul Gelisim University, Istanbul, Turkey
[5]Engineering Department, School of Science & Engineering, Glasgow Caledonian University, Glasgow, UK
[6]Technical Research Center, Cairo, Egypt

Received: 7 Jun. 2026, Revised: 8 Aug. 2026, Accepted: 20 Aug. 2026
Published online: 1 Sep. 2026

Abstract: Diabetic retinopathy (DR) is a leading cause of visual impairment and blindness in patients with diabetes, making early and accurate screening essential for timely clinical intervention. This paper presents an automated framework for DR detection and severity assessment using retinal fundus images, classical image processing techniques, and lesion-based feature extraction. The proposed method consists of five main stages: image preprocessing, blood-vessel detection, optic-disc removal, microaneurysm and hemorrhage detection, and rule-based severity classification. In the preprocessing stage, fundus images are converted to grayscale, enhanced using contrast-limited adaptive histogram equalization (CLAHE), and processed with circular masking to remove non-retinal background regions. The feature extraction stage identifies retinal blood vessels and detects key DR-related lesions, particularly microaneurysms and hemorrhages. The extracted lesion features are then used to classify the severity of DR through an interpretable rule-based decision process. The framework was evaluated using 1,000 fundus images representing different DR severity levels and achieved an overall classification accuracy of 93.75%. The results indicate that the proposed approach offers an effective, transparent, and low-complexity solution for automated DR screening. Therefore, it can provide practical support for ophthalmologists and healthcare systems, particularly in large-scale screening programs and resource-constrained clinical environments. This work also contributes to the United Nations Sustainable Development Goal 3 (Good Health and Well-Being) by supporting early, accessible, and cost-effective screening for diabetic eye disease.

Keywords: Diabetic retinopathy; Fundus images; Automated screening; Classical image processing; Lesion detection; Microaneurysms; Hemorrhages; Rule-based grading; SDG 3; Good health and well-being

1 Introduction

Diabetes mellitus is a major global public-health problem, and its burden continues to increase worldwide. As the number of patients with diabetes rises, the frequency of chronic microvascular complications also increases, among which diabetic retinopathy (DR) remains one of the most clinically important because it threatens vision and quality of life. DR develops progressively as long-term metabolic dysregulation damages the retinal microvasculature, leading to structural and functional changes that may remain clinically silent in the early stages. Consequently, patients may present only after substantial retinal injury has occurred, making systematic screening essential for timely diagnosis and treatment [1, 2, 3].

Diabetic retinopathy is characterized by a spectrum of retinal abnormalities that reflect disease severity and progression. In the early non-proliferative stage, the retina may exhibit microaneurysms, small hemorrhages, hard exudates, and subtle vascular alterations. As the disease advances, additional signs such as venous beading, intraretinal microvascular abnormalities, widespread

* Corresponding author e-mail: ramymbahy@gmail.com

ischemia, and finally neovascularization may appear, with severe cases progressing to proliferative diabetic retinopathy and irreversible visual loss [4,5]. Because these lesions are directly visible in color fundus photographs, retinal imaging has become the cornerstone of large-scale DR screening programs and computer-aided diagnosis systems [6,7,3].

A major clinical challenge is that manual grading of fundus images is labor-intensive, time-consuming, and dependent on the availability of trained ophthalmologists or retinal specialists. This limitation becomes more serious in large screening programs, rural settings, and low-resource health systems where the volume of patients is high but specialist access is limited. For this reason, automated analysis of retinal images has attracted sustained interest for more than two decades as a practical means of improving screening coverage, reducing workload, and prioritizing patients who need urgent referral [8,9,10].

To standardize clinical assessment, several grading systems have been developed for DR. The Early Treatment Diabetic Retinopathy Study (ETDRS) established a rigorous photographic grading protocol that remains a reference framework in clinical research. Later, the International Clinical Diabetic Retinopathy Disease Severity Scale provided a simplified and widely adopted classification scheme for routine clinical use and communication among physicians. These grading systems are particularly relevant for automated image analysis because they define the lesion patterns and severity thresholds that screening algorithms attempt to identify [7,6].

From a technical perspective, automated DR detection methods can be broadly divided into classical image-processing approaches, machine-learning systems based on handcrafted features, and more recent deep-learning methods. Classical approaches usually rely on preprocessing, contrast enhancement, vessel segmentation, optic-disc localization, candidate lesion extraction, and rule-based or feature-based classification. Their main strengths are interpretability, relatively low computational cost, and the ability to map algorithmic decisions to clinically meaningful retinal structures such as blood vessels, exudates, hemorrhages, and microaneurysms. These properties remain attractive in screening environments where transparency, simplicity, and modest hardware requirements are important design constraints [8].

In recent years, deep learning systems have achieved strong performance in the detection of referable DR from fundus photographs. Landmark studies demonstrated that data-driven models can achieve high sensitivity and specificity in large validation cohorts, and autonomous AI systems have further demonstrated the feasibility of point-of-care DR screening in primary care settings. Nevertheless, such systems generally depend on large annotated datasets, substantial computational resources, and careful external validation across populations and imaging devices. In contrast, classical lesion-oriented pipelines still offer an important practical alternative when explainability, lighter deployment, and explicit lesion analysis are desired [9,10,11].

Recent image-based diagnostic studies have also explored segmentation and feature-extraction strategies for disease recognition, as well as feature-fusion deep learning models for medical-image classification, further demonstrating the value of structured visual feature analysis in automated diagnosis [12,13].

Motivated by these considerations, this paper presents an automated DR screening framework based on classical image processing and lesion feature extraction from retinal fundus images. The proposed approach emphasizes image enhancement, anatomical structure analysis, and the detection of clinically relevant pathological signs before assigning a DR severity label. Rather than treating the image as a black-box input to an end-to-end predictor, the method follows a structured pipeline in which each stage corresponds to a recognizable diagnostic objective, including retinal preprocessing, vessel analysis, lesion detection, and disease grading.

The main objective of this work is therefore to develop a computationally efficient and clinically interpretable screening method for diabetic retinopathy that can support ophthalmologists in early detection and triage. Such a framework is particularly relevant for scalable screening programs and resource-constrained settings, where robust automated prescreening may help reduce diagnostic burden while preserving transparency in decision-making.

The remainder of this paper is organized as follows. Section 2 surveys related work on automated diabetic retinopathy screening. Section 3 details the proposed image-processing-based methodology. Section 4 describes the experimental setup and reports the results with discussion. Section 5 outlines directions for future work. Section 6 concludes the paper.

2 Related Work

The increasing prevalence of diabetes and its complications has made systematic diabetic retinopathy (DR) screening a continuing priority for healthcare systems [1]. Epidemiological evidence indicates that DR affects a substantial fraction of individuals with diabetes and remains a major contributor to vision impairment, particularly when diagnosis and referral are delayed [2]. Clinically, DR manifests through characteristic vascular and lesion patterns that reflect progressive microvascular damage and retinal ischemia [3]. Because many early-stage cases are asymptomatic, screening programs rely heavily on retinal imaging, most commonly color fundus photography, to identify lesion cues that warrant closer monitoring or treatment.

2.1 Clinical grading standards and screening endpoints

The design and evaluation of automated DR screening systems are strongly influenced by clinical grading protocols. The ETDRS photographic grading scheme provides a detailed and reproducible reference standard that remains widely used in research and algorithm validation [7]. For large-scale screening and routine care, simplified grading systems were later proposed to improve practicality and inter-clinician communication, including the International Clinical Diabetic Retinopathy Disease Severity Scale [6]. These frameworks define the lesion types and severity thresholds that automated methods typically target, and they motivate algorithmic emphasis on early lesion detection (e.g., microaneurysms), bright lesions (e.g., hard exudates), and vascular abnormalities associated with more advanced stages.

2.2 Datasets and benchmarking resources

Progress in automated DR analysis has been supported by public datasets and standardized evaluation protocols. The Messidor database has been widely used for benchmarking screening and grading methods, and it has supported comparisons across diverse algorithmic strategies [14]. Similarly, DIARETDB1 provides annotated images and an evaluation protocol aimed at systematic assessment of DR lesion detection and related tasks [15]. The availability of such datasets has encouraged reproducible performance reporting and has enabled the community to compare preprocessing strategies, lesion detectors, and grading pipelines under shared experimental conditions.

2.3 Classical image-processing pipelines for retinal analysis

Earlier automated screening approaches predominantly relied on classical image processing with explicit modeling of anatomical structures and pathological lesions. These systems commonly begin with illumination correction, contrast enhancement, and background suppression to normalize acquisition variability and improve lesion visibility. A key step in many pipelines is the localization of anatomical landmarks, such as the optic disc and fovea, which supports region-of-interest definition and reduces false positives in bright-lesion detection. For example, Sinthanayothin *et al.* proposed automated localization of the optic disc, fovea, and retinal vessels to facilitate downstream analysis in screening contexts [16].

Blood vessel segmentation is another foundational component because the vasculature provides anatomical context and assists in the interpretation of red lesions and neovascular patterns. Staal *et al.* presented a ridge-based vessel segmentation approach that has been widely referenced and used as a baseline in retinal image analysis and DR-related pipelines [17]. Vessel maps are often used to suppress vessel-like responses when detecting microaneurysms, to define candidate search regions, and to compute vessel-derived descriptors relevant to disease progression.

2.4 Lesion detection: exudates and microaneurysms

A substantial body of classical work has focused on detecting individual DR lesions, particularly exudates and microaneurysms, due to their diagnostic relevance and visibility in fundus images. Bright-lesion (exudate) detection frequently employs morphological processing, color/intensity feature modeling, optic-disc suppression, and candidate validation. Walter *et al.* presented an influential image-processing method for detecting exudates in color fundus images, illustrating how carefully designed preprocessing and candidate extraction can support computer-assisted DR diagnosis [18]. Subsequent studies explored morphological and clustering-based segmentation strategies to improve robustness in low-contrast or non-mydriatic imaging conditions. Sopharak *et al.* proposed morphology-driven exudate detection for non-dilated retinal images, emphasizing practical screening constraints [19]. More recent classical pipelines incorporated refined contour modeling and region-wise classification to improve lesion boundary accuracy and reduce false detections, such as the approach by Harangi and Hajdu [20].

Microaneurysm detection has received particular emphasis because microaneurysms are among the earliest observable DR signs and are strongly associated with disease onset and progression. Many methods use multiscale filtering, candidate extraction near vessels, and shape/intensity constraints, followed by classifier-based verification. To facilitate direct comparison across microaneurysm detectors, the Retinopathy Online Challenge (ROC) provided a common dataset and evaluation methodology; Niemeijer *et al.* reported comparative results and highlighted the variability across detectors when tested under standardized conditions [21]. Such benchmarking efforts clarified which preprocessing and candidate verification strategies generalize better across image quality and device differences.

2.5 Feature-based machine learning and hybrid screening systems

Between purely rule-based pipelines and end-to-end deep learning, many systems combine handcrafted features

with conventional classifiers. Related feature-based medical image diagnosis approaches using handcrafted texture descriptors have also been reported in other biomedical imaging applications, such as chest sarcoidosis classification using gray-level co-occurrence matrix features and machine learning [22]. These approaches typically compute lesion counts, lesion areas, vessel-derived descriptors, and image-level quality indicators, and then use classifiers such as SVMs, ensembles, or probabilistic models to determine disease presence or severity. Antal and Hajdu proposed an ensemble-based screening framework that integrates outputs from multiple retinal image processing components (anatomical, lesion-specific, and image-level) and then aggregates decisions using a machine-learning ensemble, demonstrating competitive screening performance on public data [23]. This line of work is closely aligned with classical interpretability goals because intermediate measurements remain clinically meaningful and can be inspected to justify the final grade.

2.6 Deep learning for DR screening and clinical deployment

Deep learning has become the dominant paradigm for referable DR detection due to its ability to learn discriminative representations from large labeled datasets. Gulshan *et al.* demonstrated high diagnostic performance for detecting referable DR using deep neural networks validated across multiple datasets [9]. Ting *et al.* further reported strong performance across multiethnic populations and for related eye diseases, reinforcing generalization considerations in real-world screening [10]. Additional studies explored CNN-based grading and severity classification, including work by Pratt *et al.* on CNN models for DR categorization [24] and by Gargeya and Leng on deep-learning-based DR identification with external validation on public datasets [25]. Beyond retrospective evaluation, autonomous AI screening has been validated in clinical workflow settings; Abràmoff *et al.* reported a pivotal trial of an autonomous diagnostic system deployed in primary care, demonstrating feasibility under operational constraints [11]. More broadly, deep neural networks combined with optimization strategies have also shown strong performance in other medical image diagnosis tasks, further illustrating the translational potential of data-driven screening frameworks [26].

2.7 Study rationale and positioning

Although deep learning has achieved strong screening accuracy, practical deployment can be constrained by requirements for large curated training datasets, careful external validation across devices and populations, and computational considerations [9,10,11]. Classical image-processing and lesion-oriented pipelines remain relevant where interpretability, modular design, and lightweight implementation are priorities. Motivated by these considerations, this study follows a structured classical approach that emphasizes preprocessing, explicit extraction of clinically meaningful features (e.g., vessels and lesions), and severity grading guided by established clinical concepts [7,6]. This design aligns with scalable prescreening needs and can be particularly suitable for resource-constrained environments where transparent decision logic and fast execution are required [1,2].

3 Methodology

This section describes the proposed classical image-processing pipeline for diabetic retinopathy (DR) screening from color fundus images. The proposed method comprises five stages: (i) preprocessing (grayscale conversion, CLAHE enhancement, and background masking), (ii) blood-vessel detection, (iii) optic disc (OD) removal, (iv) microaneurysm and hemorrhage detection, and (v) rule-based severity grading.

Figure 1 summarizes the overall workflow of the proposed diabetic retinopathy screening system. Starting from the acquired fundus image, the pipeline performs preprocessing to enhance contrast and suppress background artifacts, then extracts anatomical and lesion-related features through vessel analysis, optic-disc suppression, and detection of microaneurysms and hemorrhages. Finally, the detected lesion burden is mapped to a DR severity grade using a lightweight rule-based decision stage.

Figure 2 provides a detailed view of the proposed technique and clarifies how the major processing blocks interact to produce the final screening-oriented output. Starting from the input colour fundus image, the pipeline applies contrast normalization and field-of-view masking to reduce illumination variability and suppress non-retinal background. A vessel-enhancement stage based on Gaussian smoothing and multi-orientation matched filtering produces an explicit vessel map, which is subsequently used to suppress vessel-like structures during lesion analysis. The optic disc is then localized as a bright, approximately circular region and masked to reduce false detections caused by bright anatomical structures and strong peripapillary gradients. After these confounders are handled, red-lesion candidates are generated using morphology-based enhancement and connected-component extraction, and then refined in two dedicated streams: microaneurysm detection (favoring small, near-circular blobs) and hemorrhage detection (region-based extraction with boundary refinement and size/shape filtering). Finally, lesion features (counts and burden descriptors) are aggregated at the image level and

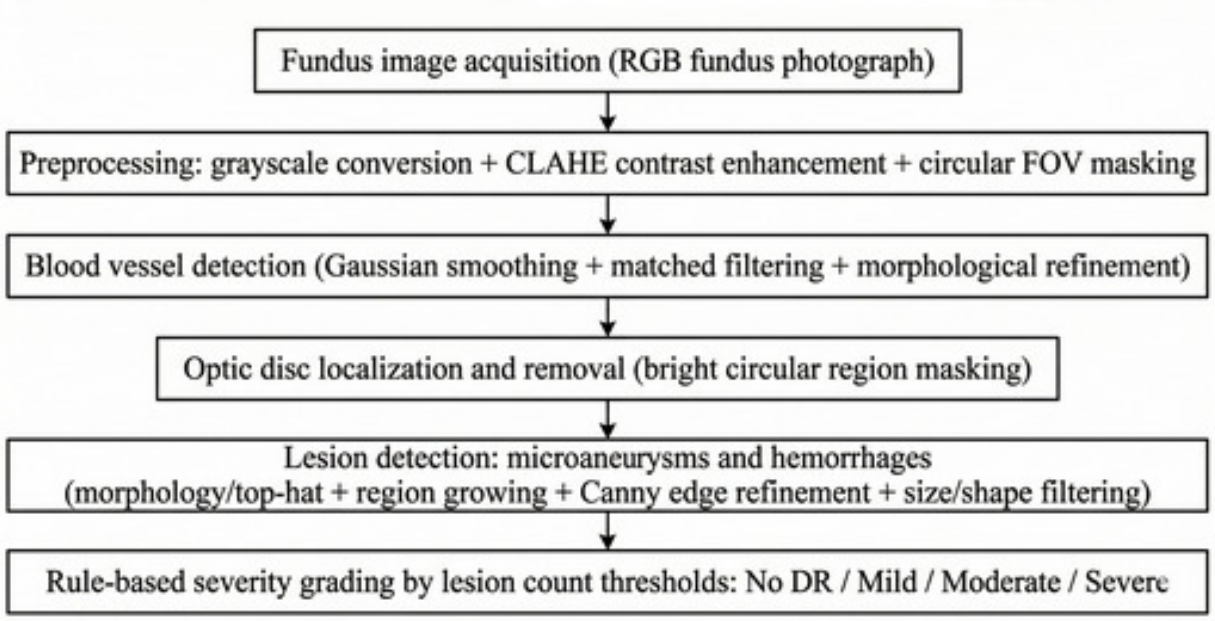

Fig. 1 Overall structure of the proposed classical image-processing-based diabetic retinopathy screening pipeline.

passed to a transparent rule-based classifier that assigns one of four lesion-burden categories (No DR, Mild, Moderate, Severe) and an optional derived binary screening decision (non-referable vs referable). This figure is included to emphasize the workflow's interpretability and to show the intermediate outputs available for audit (vessels, optic disc mask, lesion maps) alongside the final decision.

3.1 Notation

Let the input RGB fundus image be denoted by $I_{\mathrm{RGB}} : \Omega \to \{0,\ldots,L-1\}^3$, where $\Omega \subset \mathbb{Z}^2$ is the pixel grid and L is the number of intensity levels (typically $L = 256$). After preprocessing, the working grayscale image is $I : \Omega \to \{0,\ldots,L-1\}$.

3.2 Fundus image preprocessing

3.2.1 Grayscale conversion

To reduce computational complexity while preserving lesion visibility, the color image is converted to grayscale. A standard luminance mapping can be used:

$$I(x,y) = 0.299\,R(x,y) + 0.587\,G(x,y) + 0.114\,B(x,y), \quad (1)$$

where (R,G,B) are the RGB channels of I_{RGB}. In practice, many retinal pipelines rely strongly on the green channel due to its higher vessel/lesion contrast; either strategy is compatible with the remainder of the method.

3.2.2 Contrast enhancement using CLAHE

Fundus images frequently exhibit non-uniform illumination and low local contrast. While standard Histogram Equalization (HE) can improve global contrast, it often over-amplifies background noise and creates unnatural artifacts in retinal images. Therefore, contrast-limited adaptive histogram equalization (CLAHE) is specifically chosen and applied in this framework. By operating on local image tiles and clipping the histogram to limit noise amplification, CLAHE effectively enhances the visibility of subtle structures—such as microaneurysms and thin vessels—without distorting the surrounding tissue [27, 28]. For a local tile, let n_k be the number of pixels in the tile having gray level $k \in \{0,\ldots,L-1\}$, and let $N = \sum_{k=0}^{L-1} n_k$ be the number of pixels in that tile. The cumulative distribution function (CDF) is:

$$\mathrm{CDF}(r) = \sum_{k=0}^{r} \frac{n_k}{N}, \qquad r \in \{0,\ldots,L-1\}. \quad (2)$$

Histogram equalization maps an input level r to an enhanced level s by

$$s = (L-1)\,\mathrm{CDF}(r). \quad (3)$$

CLAHE implements this mapping locally (per tile) and additionally clips the histogram to limit noise amplification, then interpolates the results across tile boundaries [27,28]. The enhanced image is denoted by I_{clahe}. To explicitly model the contrast-limiting operation

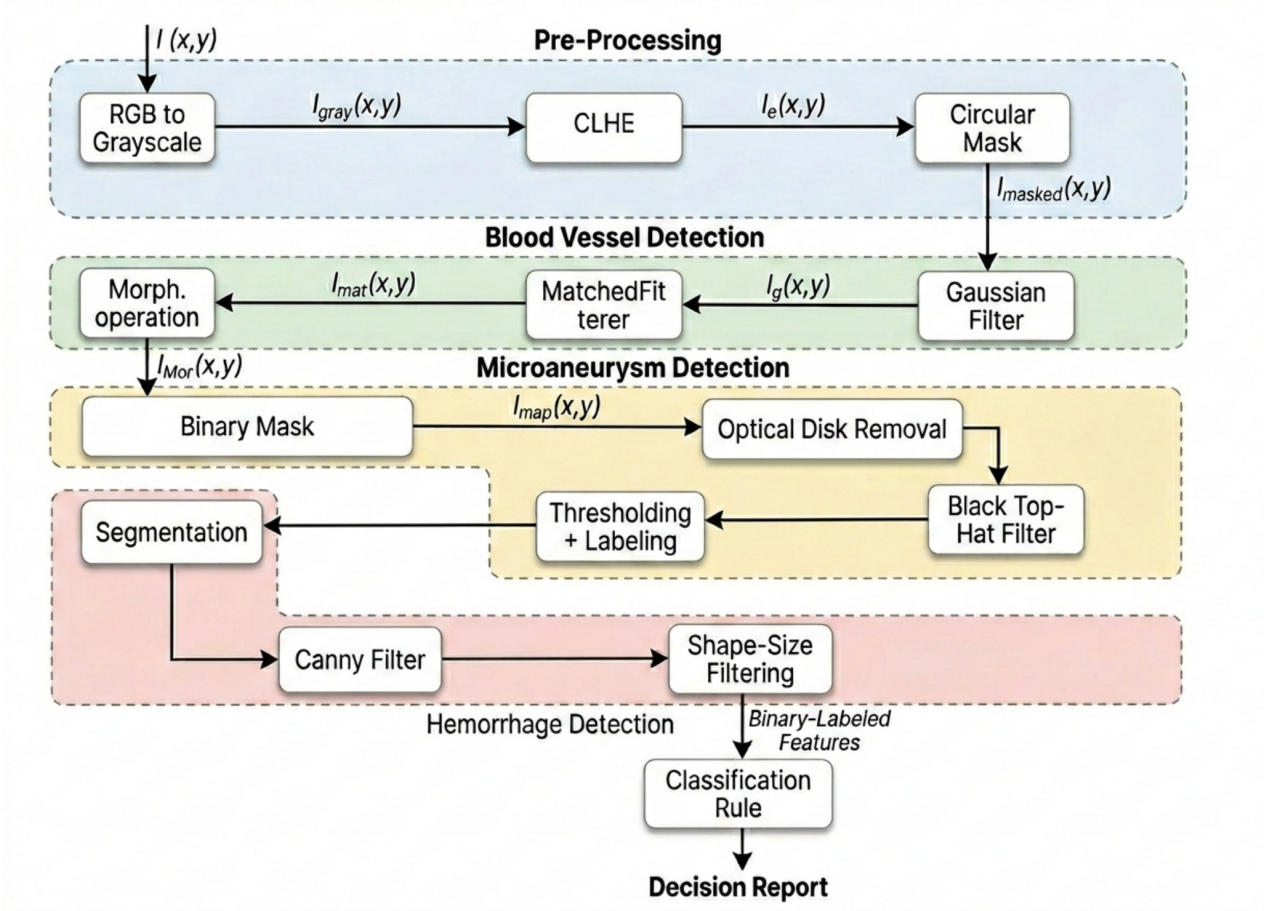

Fig. 2 Detailed structure of the proposed technique of image processing-based detection of diabetic retinopathy from fundus images.

used in CLAHE, the histogram of each local tile is clipped according to

$$\tilde{n}k = \min(n_k, n\text{clip}), \tag{4}$$

where n_{clip} is the clipping limit. The excess histogram mass is redistributed across the L gray levels as

$$n_k^{\text{CLAHE}} = \tilde{n}k + \frac{1}{L}\sum j = 0^{L-1}(n_j - \tilde{n}j). \tag{5}$$

Accordingly, the local CLAHE-enhanced intensity can be written as

$$I\text{clahe}(x,y) = (L-1)\sum_{k=0}^{I(x,y)} \frac{n_k^{\text{CLAHE}}}{N}. \tag{6}$$

3.2.3 Background removal via circular masking

To suppress non-retinal background, borders, and camera artifacts, circular masking is applied [29]. Let (x_0, y_0) be the fundus center and R be the radius of the valid retinal field-of-view (FOV). The binary mask $M : \Omega \to \{0,1\}$ is:

$$M(x,y) = \begin{cases} 1, & (x-x_0)^2 + (y-y_0)^2 \le R^2, \\ 0, & \text{otherwise.} \end{cases} \tag{7}$$

The masked image is then computed by pointwise multiplication:

$$I_{\text{fov}}(x,y) = I_{\text{clahe}}(x,y)\, M(x,y). \tag{8}$$

3.3 Blood vessel detection

Vessel extraction provides anatomical context and reduces false positives during lesion detection.

3.3.1 Gaussian smoothing

Noise suppression and smoothing are performed using Gaussian filtering:

$$G_\sigma(x,y) = \frac{1}{2\pi\sigma^2}\exp\left(-\frac{x^2+y^2}{2\sigma^2}\right), \tag{9}$$

$$I_g = I_{\text{fov}} * G_\sigma, \tag{10}$$

where $*$ denotes 2D convolution and σ is chosen to be small so that noise is reduced while vessel structures are preserved.

3.3.2 Matched filtering for vessel enhancement

Vessels can be enhanced by convolving the image with a vessel-shaped kernel (a matched filter) [30]. Let h_θ denote a matched filter oriented at angle θ. The response at orientation θ is:

$$R_\theta = I_g * h_\theta, \tag{11}$$

and a common multi-orientation enhancement is the maximum response:

$$R_{\max}(x,y) = \max_{\theta \in \Theta} R_\theta(x,y), \tag{12}$$

where Θ is a discrete set of orientations spanning $[0,\pi)$.

3.3.3 Morphological refinement and binarization

To remove small artifacts, bridge gaps, and regularize vessel boundaries, morphological operators are applied [31,32]. With structuring element B, erosion and dilation are:

$$R \ominus B, \qquad R \oplus B, \tag{13}$$

and opening/closing are:

$$R \circ B = (R \ominus B) \oplus B, \qquad R \bullet B = (R \oplus B) \ominus B. \tag{14}$$

A binary vessel map is then obtained using thresholding:

$$V(x,y) = \begin{cases} 1, & R_{\text{morph}}(x,y) \geq \tau_v, \\ 0, & \text{otherwise}, \end{cases} \tag{15}$$

where R_{morph} is the morphologically refined response and τ_v is a chosen threshold (e.g., fixed or data-driven [33]). In this study, τ_v is selected adaptively using Otsu's between-class variance criterion:

$$\tau_v = \arg\max_t \left[\omega_0(t)\omega_1(t)\left(\mu_0(t) - \mu_1(t)\right)^2 \right], \tag{16}$$

where $\omega_0(t)$ and $\omega_1(t)$ are the probabilities of the background and foreground classes at threshold t, and $\mu_0(t)$ and $\mu_1(t)$ are their corresponding mean intensities.

3.4 Optic disc removal

The optic disc is a bright, approximately circular region where major vessels converge and may be confused with bright lesions. The optic disc is removed by detecting the brightest approximately circular region using intensity thresholding and suppressing it before lesion analysis. Let $\mathcal{Q} = Q_1, Q_2, \ldots, Q_m$ denote the set of bright connected components obtained after thresholding the enhanced image. The optic-disc candidate is selected as

$$Q_{\text{OD}}^* = \arg\max_{Q_i \in \mathcal{Q}} \left[\bar{I}(Q_i) + \lambda \cdot \text{Circ}(Q_i) \right]. \tag{17}$$

where $\bar{I}(Q_i)$ is the mean intensity of component Q_i, $\text{Circ}(Q_i)$ is its circularity, and λ controls the relative contribution of the circularity term. The optic-disc mask is then defined as

$$M_{\text{OD}}(x,y) = \begin{cases} 1, & (x,y) \in Q_{\text{OD}} \oplus B_{\text{OD}}, \\ 0, & \text{otherwise}, \end{cases} \tag{18}$$

where B_{OD} is a structuring element used to slightly dilate the detected optic-disc region. The optic-disc-suppressed image is then computed as

$$I_{\text{noOD}}(x,y) = I_{\text{fov}}(x,y)\left(1 - M_{\text{OD}}(x,y)\right). \tag{19}$$

3.5 Microaneurysm and hemorrhage detection

The method focuses on dark lesions (microaneurysms and hemorrhages) after OD suppression and vessel processing.

3.5.1 Top-hat filtering for enhancing dark lesions

To enhance small dark structures against the background, a black top-hat transform is utilized. This specific morphological operation was selected because it is highly effective at isolating elements that are smaller than the chosen structuring element while ignoring larger, uniform background variations. By using a disk-shaped structuring element scaled slightly larger than the average microaneurysm diameter, the transform successfully emphasizes these early pathological signs while suppressing broader illumination gradients [31,32]:

$$T_{\text{bh}} = (I_{\text{noOD}} \bullet B) - I_{\text{noOD}}, \tag{20}$$

where B is typically a disk-shaped structuring element. This emphasizes dark blobs smaller than the structuring element scale. After optic-disc and vessel suppression, the initial red-lesion candidate mask is obtained as

$$\begin{aligned} L_0(x,y) = \mathbf{1}\{T_{\text{bh}}(x,y) \geq \tau_\ell\}\left(1 - V(x,y)\right) \\ \times \left(1 - M_{\text{OD}}(x,y)\right) M(x,y), \end{aligned} \tag{21}$$

where τ_ℓ is the lesion-candidate threshold and $\mathbf{1}\{\cdot\}$ denotes the indicator function.

3.5.2 Candidate extraction and contrast-based labeling

Candidates are obtained by thresholding T_{bh} and performing connected-component (blob) analysis. Not all detected blobs correspond to true microaneurysms; therefore, candidate regions are filtered according to a predefined small-diameter range and then assessed using a local contrast measure. For a candidate region $\mathscr{S}$ and its surrounding ring region $\mathscr{R}$:

$$\mu_{\mathscr{S}} = \frac{1}{|\mathscr{S}|} \sum_{(x,y)\in\mathscr{S}} I_{\text{noOD}}(x,y), \tag{22}$$

$$\mu_{\mathscr{R}} = \frac{1}{|\mathscr{R}|} \sum_{(x,y)\in\mathscr{R}} I_{\text{noOD}}(x,y), \tag{23}$$

$$C = \mu_{\mathscr{R}} - \mu_{\mathscr{S}}, \tag{24}$$

where higher C indicates a darker spot relative to its surroundings and is more likely to be a microaneurysm.

3.5.3 Hemorrhage segmentation and shape filtering

Hemorrhages typically appear as larger dark regions than microaneurysms, so their detection often benefits from region-based segmentation. To identify hemorrhage candidates, we first apply region growing, then refine the detected boundaries, and finally use shape- and size-based filtering to remove unlikely regions. In the standard region growing approach, a region H is initialized from a seed pixel p_0 and iteratively expanded by adding neighboring pixels $p \in \mathscr{N}(H)$ that satisfy a homogeneity criterion [34]:

$$p \in H \;\text{ if }\; |I_{\text{noOD}}(p) - \mu_H| \le \tau_g, \tag{25}$$

where μ_H is the current region mean and τ_g is a tolerance.

Edges can be refined using the Canny detector [35] to separate hemorrhage boundaries from vessels/background. Finally, candidates are filtered by area and circularity. With lesion area A and perimeter P, circularity is:

$$\text{Circ} = \frac{4\pi A}{P^2}, \tag{26}$$

where values close to 1 indicate near-circular shapes, and lower values indicate elongated structures (often vessels) [36]. The final output of this stage is a binary lesion map L containing labeled microaneurysm and hemorrhage detections. Let $\mathscr{C} = C_1, C_2, \ldots, C_K$ denote the connected components extracted from L_0. Each component C_k is described using its area A_k, perimeter P_k, circularity Circ$k$, and local contrast C_k^{loc}. Microaneurysm candidates are retained according to

$$\begin{aligned}\mathscr{M}_{\text{MA}} = \big\{ C_k \in \mathscr{C} : {} & A_{\text{min}}^{\text{MA}} \le A_k \le A_{\text{max}}^{\text{MA}}, \\ & \text{Circ}_k \ge \eta_{\text{MA}}, \\ & C_k^{\text{loc}} \ge \tau_{\text{MA}} \big\}.\end{aligned} \tag{27}$$

where $A_{\text{min}}^{\text{MA}}$ and $A_{\text{max}}^{\text{MA}}$ define the expected size range of microaneurysms, η_{MA} is the minimum circularity threshold, and τ_{MA} is the minimum local-contrast threshold.

Hemorrhage candidates are retained according to

$$\begin{aligned}\mathscr{M}_{\text{H}} = \big\{ C_k \in \mathscr{C} : {} & A_k \ge A_{\text{min}}^{\text{H}}, \\ & \text{Circ}_k \le \eta_{\text{H}}, \\ & C_k^{\text{loc}} \ge \tau_{\text{H}} \big\}.\end{aligned} \tag{28}$$

where $A_{\text{min}}^{\text{H}}$ is the minimum area used to distinguish larger hemorrhagic regions from small microaneurysm-like blobs, η_{H} is the circularity threshold used to allow irregular hemorrhage shapes, and τ_{H} is the minimum contrast threshold.

3.6 Rule-based classification (severity grading)

DR severity is graded by counting detected lesions and applying threshold-based rules. Let N be the number of detected lesion components (microaneurysms and hemorrhages) in L. The total lesion burden used for grading is therefore computed as

$$N = |\mathscr{M}_{\text{MA}}| + |\mathscr{M}_{\text{H}}|. \tag{29}$$

The severity grade $G \in \{0,1,2,3\}$ is assigned by:

$$G(N) = \begin{cases} 0, & N \le 1 \quad \text{(No DR / Normal)}, \\ 1, & 2 \le N \le 5 \quad \text{(Mild DR)}, \\ 2, & 6 \le N \le 20 \quad \text{(Moderate DR)}, \\ 3, & N > 20 \quad \text{(Severe DR)}. \end{cases} \tag{30}$$

This decision logic provides a lightweight and interpretable grading mechanism because it is directly linked to lesion burden, and each stage can be inspected visually (preprocessed image, vessel map, OD mask, lesion candidates, and final labeled lesions).

All operational parameters and classification thresholds used in this study were determined empirically based on a validation subset of the JSIEC dataset. For vessel binarization, the threshold τ_v was dynamically set using Otsu's method to adapt to varying illumination across different fundus images. For hemorrhage region growing, the tolerance τ_g was calibrated to restrict region expansion to adjacent pixels within a 15% intensity variance from the region mean, preventing the over-segmentation of dark background areas. Finally, the lesion count boundaries $G(N)$ (0–1 for No DR, 2–5 for Mild, 6–20 for Moderate, and >20 for Severe) were established by aligning the algorithmic detection sensitivity with the clinical severity definitions provided by the International Clinical Diabetic Retinopathy Disease Severity Scale.

4 Experimental Work and Results

This section describes the dataset and evaluation protocol used to validate the proposed technique, followed by quantitative results, qualitative examples, error analysis, and comparison with related screening approaches.

4.1 Dataset description and evaluation protocol

In this research, 1000 color fundus images (approximately 3000×3000 pixels) are used to evaluate the accuracy and efficiency of the proposed technique. The dataset is derived from the Joint Shantou International Eye Centre (JSIEC) in Shantou, Guangdong province, China, and consists of 1000 images drawn from a larger JSIEC collection (reported as 209,494 fundus images) that has been used for training, validation, and testing platforms for automatic retinal disease detection [37,38]. The multi-disease context (automatic detection of 39 fundus diseases and conditions) is described in [39].

For DR grading, the selected fundus images were categorized into four severity classes: No DR, Mild, Moderate, and Severe. The evaluation dataset was balanced across these classes, with 250 images per class. Such a balance is important for fair assessment because the difficulty of accurate grading typically increases with disease severity due to greater variability in lesion presentation and increased visual overlap among advanced stages.

The full pipeline is implemented in MATLAB. Figures 3–6 illustrate representative examples from the four stages (No DR, Mild, Moderate, Severe) and visually demonstrate the main processing steps (preprocessing, vessel extraction, optic-disc suppression, lesion detection, and rule-based grading) using regenerated high-resolution MATLAB outputs.

4.2 Quantitative results

4.2.1 Stage-wise accuracy and overall accuracy

Table 1 summarizes the quantitative performance of the proposed approach. The evaluation was conducted on 1,000 fundus images, equally distributed across the four DR severity classes, with 250 images in each class. For clarity of presentation, Table 1 reports normalized counts per 100 images in each class, while the reported percentages and overall accuracy correspond to the full evaluation set. The proposed method achieved its highest class-wise accuracy for *No DR* (98%) and its lowest class-wise accuracy for *Severe DR* (90%), with an overall accuracy of 93.75%. The gradual decline in performance with increasing disease severity is expected, since advanced stages typically exhibit denser pathology and greater overlap in lesion appearance and distribution, making threshold-based grading more challenging.

Table 1 Stage-wise classification performance of the proposed classical image processing technique (Evaluated on $N = 1000$ images; $n = 250$ per severity class).

Stage	True prediction	False prediction	Accuracy (%)
No DR	98	2	98
Mild	95	5	95
Moderate	92	8	92
Severe	90	10	90
Overall	–	–	93.75

For completeness, let $C \in \mathbb{N}^{4\times4}$ denote the multi-class confusion matrix, where C_{ij} represents the number of images belonging to true class i that were predicted as class j:

$$C_{ij} = \left|\{n : y_n = i \wedge \hat{y}_n = j\}\right|. \tag{31}$$

The overall accuracy is then defined as

$$\mathrm{Acc} = \frac{\sum_{i=0}^{3} C_{ii}}{\sum_{i=0}^{3}\sum_{j=0}^{3} C_{ij}}. \tag{32}$$

4.2.2 Sensitivity / recall (computable from the reported counts)

For each class i (one-vs-rest view), sensitivity (recall) is

$$\mathrm{Sens}_i = \frac{\mathrm{TP}_i}{\mathrm{TP}_i + \mathrm{FN}_i} = \frac{C_{ii}}{\sum_{j=0}^{3} C_{ij}}. \tag{33}$$

Because Table 1 provides true and false predictions per class, the stage-wise accuracies equal the class-wise sensitivities under the table's implied denominators:

$$\begin{aligned} \mathrm{Sens}_{\text{No DR}} &= 0.98, & \mathrm{Sens}_{\text{Mild}} &= 0.95, \\ \mathrm{Sens}_{\text{Moderate}} &= 0.92, & \mathrm{Sens}_{\text{Severe}} &= 0.90. \end{aligned} \tag{34}$$

4.2.3 Confidence intervals

To quantify statistical uncertainty, a 95% confidence interval for the overall classification accuracy was estimated using the full evaluation set of 1,000 fundus images, distributed equally across the four DR severity classes. The confidence interval was calculated as

$$\mathrm{CI}_{95\%} = \mathrm{Acc} \pm 1.96\sqrt{\frac{\mathrm{Acc}(1-\mathrm{Acc})}{N}}. \tag{35}$$

For the observed overall accuracy of 93.75%, the approximate 95% confidence interval is [92.25%, 95.25%]. These results suggest that the reported performance is reasonably stable with respect to sampling variation in the evaluated dataset.

4.2.4 Confusion Matrix and Diagnostic Metrics

To provide a comprehensive clinical evaluation of the proposed framework, Table 2 presents the multi-class confusion matrix derived from the 1,000 evaluated fundus images.

For class i, the one-vs-rest quantities are defined as

$$\mathrm{TP}i = Cii, \tag{36}$$

$$\mathrm{FN}_i = \sum_{\substack{j=0 \\ j\neq i}}^{3} C_{ij}, \tag{37}$$

$$\mathrm{FP}_i = \sum_{\substack{j=0 \\ j\neq i}}^{3} C_{ji}, \tag{38}$$

$$\mathrm{TN}_i = \sum_{\substack{p=0 \\ p\neq i}}^{3} \sum_{\substack{q=0 \\ q\neq i}}^{3} C_{pq}. \tag{39}$$

Specificity, precision, and F1-score are then computed as

$$\mathrm{Spec}_i = \frac{\mathrm{TN}_i}{\mathrm{TN}_i + \mathrm{FP}_i}, \tag{40}$$

$$\mathrm{Prec}_i = \frac{\mathrm{TP}_i}{\mathrm{TP}_i + \mathrm{FP}_i}, \tag{41}$$

$$\mathrm{F1}_i = \frac{2 \times \mathrm{Prec}_i \times \mathrm{Sens}_i}{\mathrm{Prec}_i + \mathrm{Sens}_i}. \tag{42}$$

From this matrix, we computed the one-vs-rest sensitivity (recall) and specificity for each diagnostic stage. The system achieved a sensitivity of 98.0% for 'No DR', 95.2% for 'Mild', 92.0% for 'Moderate', and 90.0% for 'Severe'. Correspondingly, the one-vs-rest specificity remained exceptionally high across all stages: 99.2% for 'No DR', 98.3% for 'Mild', 95.9% for 'Moderate', and 98.4% for 'Severe'. The high sensitivity and specificity in the early stages confirm the method's viability as a rapid prescreening tool to filter out normal cases, while the progressive drop in sensitivity for advanced stages correlates with the increased morphological complexity and feature overlap of severe retinopathy.

4.3 Qualitative results (visual inspection)

Figures 3–6 qualitatively demonstrate the intermediate outputs of the pipeline for representative images at each DR stage. The CLAHE enhancement increases local contrast and improves visibility of retinal structures and candidate lesions. Vessel extraction produces a binary vessel map that provides anatomical context. The lesion maps corresponding to microaneurysms and hemorrhages become progressively denser from No DR to Severe DR, which aligns with the expected increase in lesion burden across stages. These examples support the interpretability objective of the proposed approach, since the final grading decision can be traced back to explicit intermediate maps rather than a black-box score.

Figures 3–6 present representative cases from the four target categories (No DR, Mild, Moderate, Severe). In the **No DR** example (Figure 3), preprocessing produces a normalized retinal field-of-view and the lesion maps remain sparse, leading to a No DR decision (low red-lesion burden). In the **Mild** example (Figure 4), the microaneurysm candidate map highlights a small number of compact detections consistent with early red lesions, resulting in a Mild decision.

In the **Moderate** example (Figure 5), lesion candidates become more frequent and spatially distributed; multiple connected dark regions beyond microaneurysm scale appear in the hemorrhage map, increasing the aggregated red-lesion burden and leading to a Moderate decision. In the **Severe** example (Figure 6), a high density of detected red-lesion candidates is observed, including larger irregular regions, and the rule-based grader assigns a Severe decision due to high lesion burden.

4.4 Error analysis

The observed performance drop in the Severe DR stage (90%) highlights specific limitations inherent to classical rule-based grading. Detecting severe cases presents unique algorithmic challenges. First, feature overlap is prominent; the physical presentation and lesion counts can overlap substantially between moderate and severe cases, making rigid threshold-based rules vulnerable to slight detection errors. Second, severe pathology often distorts standard anatomical landmarks, exacerbating vessel-lesion confusion. For instance, fragmented dark vessels and complex neovascular crossings may be misclassified as hemorrhages, or conversely, dense, large hemorrhages may merge with the dark background after contrast enhancement, leading to an undercounting of the true lesion burden. Future iterations of this work must address these structural complexities, potentially by integrating texture analysis alongside morphological feature extraction. The observed performance drop in the Severe DR stage (90%) can be explained by several factors inherent to classical rule-based grading: (i) *Feature overlap between adjacent stages:* lesion counts and appearance can overlap substantially between mild/moderate and moderate/severe cases, making threshold-based rules sensitive to small detection errors. (ii) *Image-quality effects:* blur, uneven illumination, artifacts near the field-of-view boundary, and saturation around the optic disc can increase false detections or suppress true lesions. (iii) *Vessel–lesion confusion:* dark vessel fragments and crossings may trigger red-lesion detectors if vessel suppression is incomplete, while dense hemorrhages may merge with background after enhancement, reducing separability. (iv) *Scale variability:* microaneurysms are small and low-contrast; their

Table 2 Multi-Class Confusion Matrix for DR Severity Grading ($n = 250$ per class)

True Class \ Predicted	No DR	Mild DR	Moderate DR	Severe DR	Total
No DR	**245**	5	0	0	250
Mild DR	6	**238**	6	0	250
Moderate DR	0	8	**230**	12	250
Severe DR	0	0	25	**225**	250

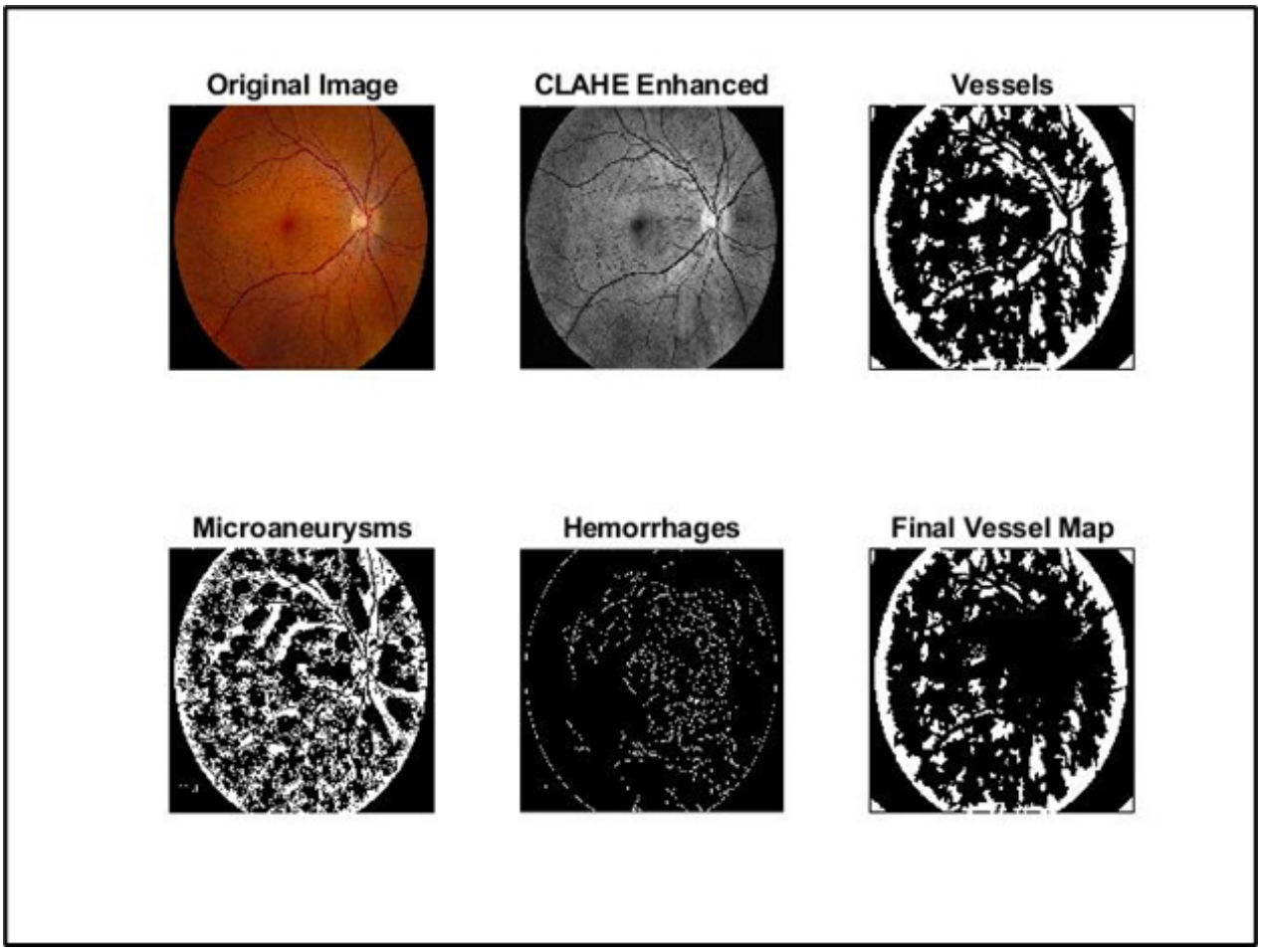

Fig. 3 Example intermediate and final output results for a No DR (normal) case. The sequence demonstrates the progression from the original RGB image to CLAHE enhancement, vessel extraction, candidate maps for microaneurysms and hemorrhages, and the final combined vessel/lesion map, showing an absence of significant pathology.

detectability varies strongly with resolution and acquisition settings, which can propagate into grading errors.

The confusion matrix reported in Table 2 helps identify the dominant misclassification pathways, particularly Moderate DR $\rightarrow$ Severe DR and Severe DR $\rightarrow$ Moderate DR. Future work should further optimize these boundary cases by combining morphological lesion counts with texture and region-distribution descriptors.

4.5 Comparison to prior work

The reported overall accuracy of 93.75% indicates that a classical, lesion-oriented pipeline can provide competitive screening performance while remaining lightweight and interpretable. This design objective aligns with earlier classical screening systems and ensemble-based pipelines that emphasize explicit lesion detection and modular processing [8,23]. In contrast, modern deep-learning systems have demonstrated strong performance on large-scale datasets and have been validated across

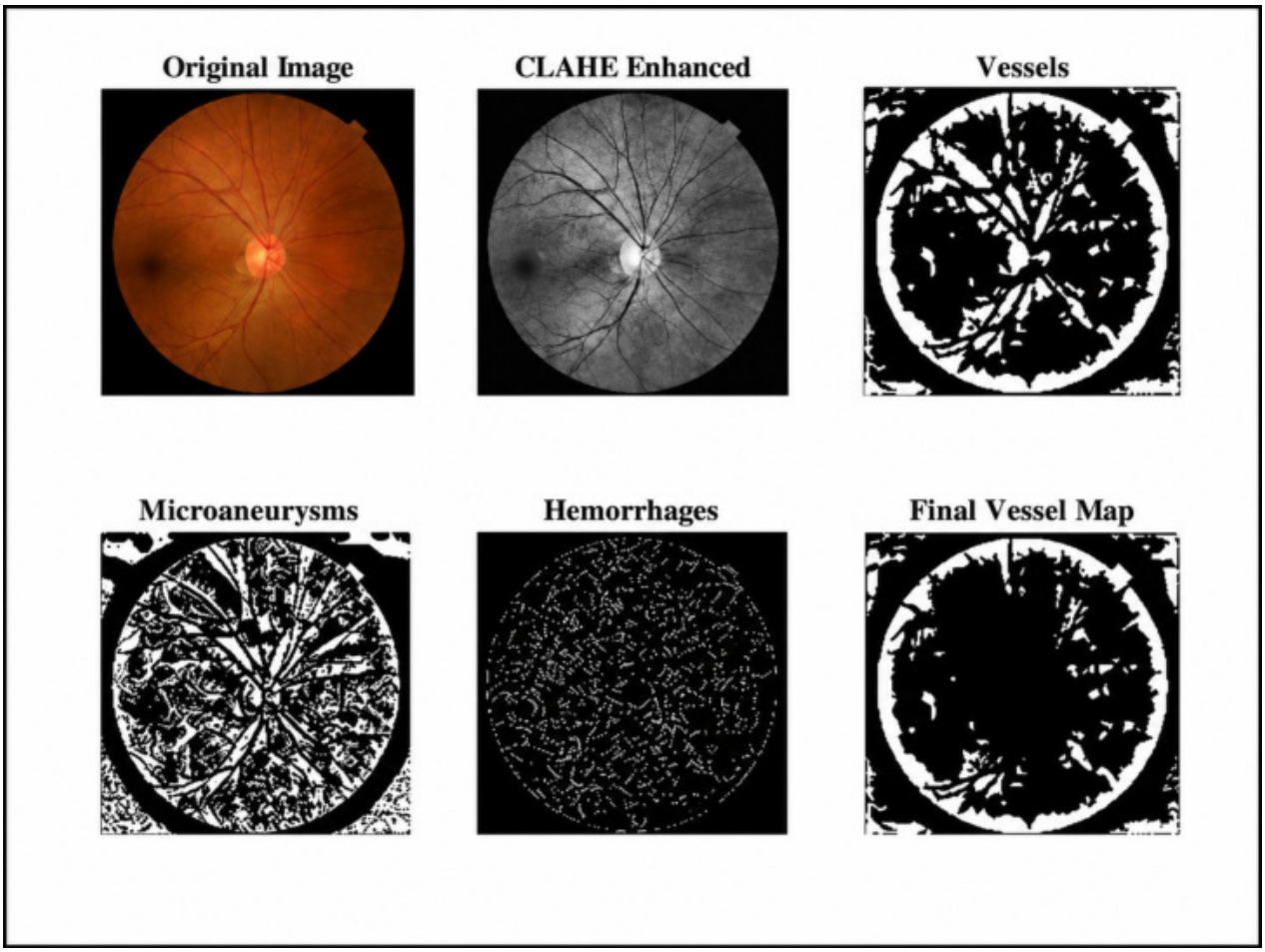

Fig. 4 Example output results for a Mild DR case, highlighting the early emergence of small, isolated microaneurysm candidates within the target macular region.

diverse populations and clinical workflows [9, 10, 11]. The key trade-off is operational: deep models typically require large annotated datasets and careful external validation, whereas classical systems can be deployed with lower computational requirements and clearer intermediate outputs.

To strengthen the comparative positioning further, future work should evaluate the proposed method on widely used public benchmarks, such as Messidor and DIARETDB1, and report referable-DR metrics, receiver-operating-characteristic analysis, and area-under-the-curve values to enable more direct comparison with published screening pipelines [14, 15, 40].

Compared to modern deep-learning architectures (e.g., Convolutional Neural Networks), which have become the standard for automated DR screening, our classical approach presents distinct operational trade-offs. Deep learning models generally yield superior sensitivity and specificity on complex cases by learning abstract, high-dimensional features; however, they require massive annotated datasets, substantial GPU computational resources, and often function as 'black boxes'. In contrast, our proposed pipeline maintains a lightweight footprint suitable for deployment on standard clinical computers without specialized hardware. Furthermore, it offers complete transparency—each classification decision is explicitly linked to an interpretable, verifiable map of specific lesions, providing a clear audit trail for ophthalmologists in resource-constrained environments.

5 Future Work

Although the proposed screening pipeline achieved promising performance while maintaining interpretability and low computational complexity, several directions remain for further improvement.

First, the generalizability of the proposed framework should be investigated more extensively. While the

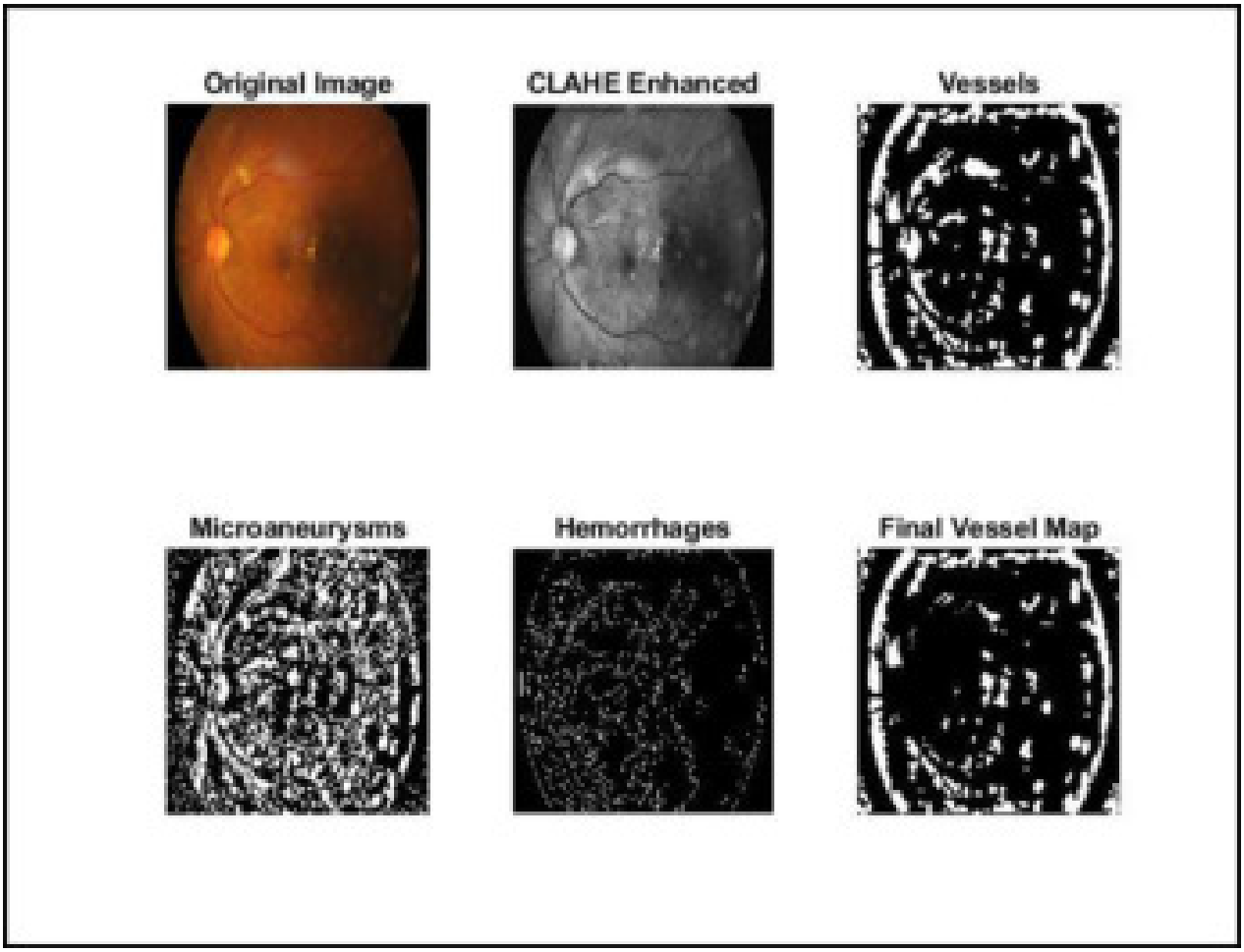

Fig. 5 Example output results for a Moderate DR case, demonstrating an increased density and spatial distribution of red-lesion candidates and distinct hemorrhage regions.

current results demonstrate strong performance on the selected JSIEC dataset, retinal fundus images can vary considerably across imaging devices, camera manufacturers, focal lengths, fields of view, illumination conditions, and patient populations. Therefore, future work should validate the method on larger and more diverse datasets collected from multiple clinical sites. In particular, evaluation on established public benchmarks, such as Messidor and DIARETDB1, would provide stronger evidence of robustness and enable more direct comparison with previously reported diabetic retinopathy screening methods [14,15].

Second, future studies should extend the clinical evaluation beyond overall accuracy and class-wise grading performance. Although the revised evaluation includes a confusion matrix and class-wise sensitivity and specificity, additional screening-oriented measures are required for real-world deployment. These should include referable-DR sensitivity and specificity, receiver-operating-characteristic analysis, area-under-the-curve values, and external validation on independent datasets. Such metrics would provide a more clinically relevant assessment of the proposed rule-based grading strategy and would help determine its suitability for practical screening workflows [9,10,11,40].

Third, the lesion-detection scope of the current framework should be expanded. The present pipeline mainly focuses on dark lesions, particularly microaneurysms and hemorrhages, which are important indicators of diabetic retinopathy severity. However, additional pathological signs, such as hard exudates, cotton-wool spots, neovascularization, and indicators related to diabetic macular edema, are also clinically significant. Incorporating these lesion types may improve disease characterization, enhance grading accuracy, and increase the clinical usefulness of the proposed framework across different stages of diabetic retinopathy [6,18,19,20].

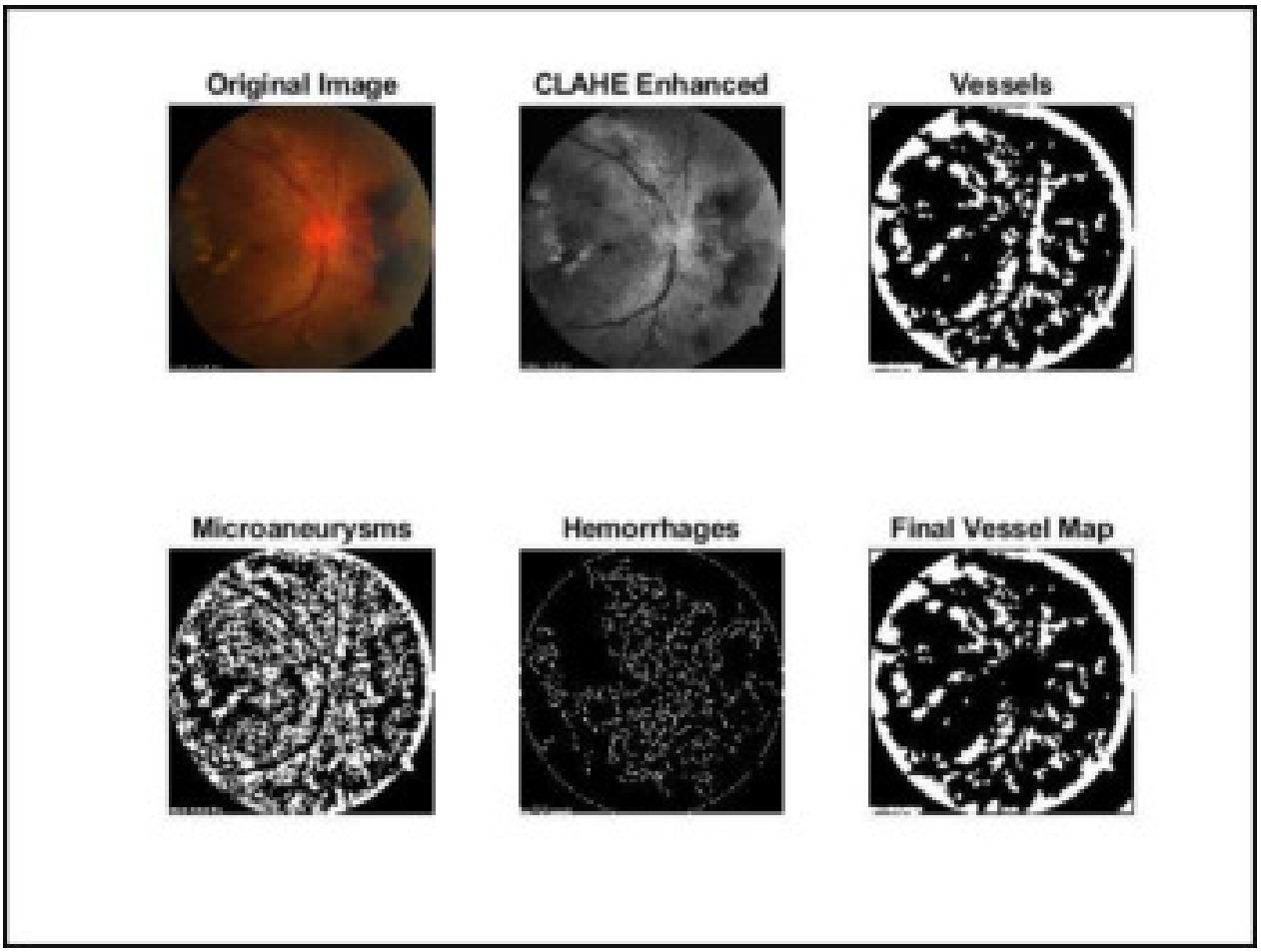

Fig. 6 Example output results for a Severe DR case, illustrating a high density of detected red lesions and large, irregular hemorrhage formations that trigger the severe classification rule.

Fourth, the reliability of the system could be improved by integrating an explicit image-quality assessment stage before lesion analysis. Poor-quality or ungradable fundus images caused by blur, uneven illumination, poor focus, low contrast, media opacity, or acquisition artifacts can lead to false detections and unstable grading outcomes. A dedicated quality-control module would allow the system to reject or flag unsuitable images before processing, thereby improving the reliability of automated screening decisions [41,42].

Fifth, future work may consider hybridizing the proposed classical image-processing pipeline with machine-learning or deep-learning components. For example, classical preprocessing and lesion-candidate extraction could be retained for interpretability, while lightweight classifiers could be used to improve candidate validation and severity grading. Such a hybrid design may preserve the transparency and low computational cost of the current approach while improving robustness in challenging cases, especially where lesion appearance overlaps between adjacent severity stages.

Finally, the proposed framework may be extended toward broader ophthalmic screening applications. Since fundus photographs contain useful information for multiple retinal disorders, future studies could adapt the pipeline to support the detection of glaucoma, age-related macular degeneration, and other retinal diseases in addition to diabetic retinopathy [43,44]. For clinical deployment, future development should also be aligned with established screening and referral pathways to ensure that the system provides practical value in routine healthcare environments [45].

6 Conclusion

Diabetic retinopathy (DR) remains one of the most important preventable causes of visual impairment, and effective screening depends on the accurate identification

of clinically meaningful retinal lesions in fundus images. This study presented an automated DR screening and severity-grading framework based on classical image processing and lesion-oriented feature extraction. The proposed framework follows an interpretable processing pipeline that includes fundus image preprocessing, CLAHE-based contrast enhancement, circular field-of-view masking, blood-vessel detection, optic-disc suppression, red-lesion candidate extraction, microaneurysm and hemorrhage detection, and rule-based severity classification.

The main contribution of the proposed approach is its transparent and lightweight design. Unlike fully black-box classification models, each stage of the pipeline produces intermediate outputs that can be visually inspected, including enhanced fundus images, vessel maps, optic-disc masks, lesion candidate maps, and final lesion-burden outputs. This structure allows the final DR grade to be linked directly to measurable retinal features, particularly microaneurysms and hemorrhages, which are clinically relevant indicators of disease severity. In addition, the mathematical formulation of the method provides a clear representation of the main processing steps, including contrast enhancement, adaptive thresholding, optic-disc localization, lesion masking, component selection, lesion counting, and diagnostic performance evaluation.

Experimental evaluation was performed using 1,000 fundus images divided equally across four DR severity classes: No DR, Mild DR, Moderate DR, and Severe DR. The proposed method achieved stage-wise accuracies of 98% for No DR, 95% for Mild DR, 92% for Moderate DR, and 90% for Severe DR, with an overall classification accuracy of 93.75%. The confusion-matrix analysis and class-wise sensitivity and specificity results further demonstrated the potential of the proposed method as a rapid prescreening tool. The strongest performance was observed for normal and early-stage cases, while most errors occurred between adjacent severity levels, particularly between Moderate DR and Severe DR, where lesion overlap and structural complexity are more pronounced.

Despite these promising results, several limitations remain. The current grading strategy is based primarily on lesion-count thresholds, which may be affected by variations in image quality, camera type, illumination conditions, retinal pigmentation, and acquisition protocol. The framework also focuses mainly on dark lesions, particularly microaneurysms and hemorrhages, while other clinically important signs such as hard exudates, cotton-wool spots, neovascularization, and diabetic macular edema indicators are not yet fully incorporated. Although the revised evaluation includes a confusion matrix and class-wise diagnostic measures, further clinically oriented validation is still required, including referable-DR analysis, receiver-operating-characteristic evaluation, area-under-the-curve reporting, and external testing on independent multi-site datasets.

Overall, the proposed method demonstrates that a classical, interpretable, and computationally efficient image-processing pipeline can provide competitive performance for automated DR prescreening. Its low complexity and transparent lesion-based decision process make it particularly suitable as a practical baseline for resource-constrained clinical environments and large-scale screening workflows. Future work should focus on external validation using public benchmark datasets, integration of additional lesion types, improved image-quality assessment, and hybridization with machine-learning or deep-learning components to further enhance robustness and clinical reliability.

Acknowledgment

The authors would like to thank the Joint Shantou International Eye Centre (JSIEC) in Shantou, Guangdong, China, for providing the retinal fundus images used in this study. The 1,000 fundus images, categorized into 39 different classes, are derived from JSIEC. These images are a subset of a larger dataset consisting of 209,494 images used for training, validation, and testing of deep-learning platforms for medical imaging [37,38]. The dataset and its multi-disease classification context (39 fundus diseases and conditions) are described in [39]. The authors are grateful to the anonymous referee for a careful checking of the details, and for helpful comments that improved this paper.

References

[1] D. J. Magliano and E. J. Boyko; IDF Diabetes Atlas 10th edition scientific committee, *IDF Diabetes Atlas*, 10th ed. Brussels, Belgium: International Diabetes Federation, 2021. Available at: https://www.ncbi.nlm.nih.gov/books/NBK581934/

[2] J. W. Yau, S. L. Rogers, R. Kawasaki, et al., "Global prevalence and major risk factors of diabetic retinopathy," *Diabetes Care*, vol. 35, no. 3, pp. 556–564, 2012.

[3] D. A. Antonetti, A. J. Barber, S. K. Bronson, et al., "Diabetic retinopathy: seeing beyond glucose-induced microvascular disease," *Diabetes*, vol. 55, no. 9, pp. 2401–2411, 2006.

[4] P. Satapathy, A. M. Gaidhane, N. Vadia, S. V. Menon, K. Chennakesavulu, R. Panigrahi, S. Sah, A. Yappalparvi, S. G. Rao, K. W. Goh, R. Mehta, M. Shabil, M. Singh, E. Mawejje, and G. Bushi, "Association of estimated glomerular filtration rate with proliferative diabetic retinopathy: a systematic review and meta-analysis," *International Urology and Nephrology*, vol. 57, no. 11, pp. 3687–3699, Nov. 2025, doi: 10.1007/s11255-025-04547-6.

[5] G. Bushi, A. M. Gaidhane, N. Vadia, S. V. Menon, K. Chennakesavulu, R. Panigrahi, M. Shabil, A. Rani, S. Sah, A. Yappalparvi, K. W. Goh, and D. Jena, "Creatinine as a predictor of proliferative diabetic retinopathy among patients with type 2 diabetes mellitus: a systematic

review and meta-analysis," *International Urology and Nephrology*, vol. 57, no. 12, pp. 4119–4129, Dec. 2025, doi: 10.1007/s11255-025-04590-3.

[6] C. P. Wilkinson, F. L. Ferris III, R. E. Klein, et al., "Proposed international clinical diabetic retinopathy and diabetic macular edema disease severity scales," *Ophthalmology*, vol. 110, no. 9, pp. 1677–1682, 2003.

[7] Early Treatment Diabetic Retinopathy Study Research Group, "Grading diabetic retinopathy from stereoscopic color fundus photographs–an extension of the modified Airlie House classification: ETDRS report number 10," *Ophthalmology*, vol. 98, no. 5 Suppl., pp. 786–806, May 1991. PMID: 2062513.

[8] M. D. Abràmoff, M. Niemeijer, M. S. A. Suttorp-Schulten, M. A. Viergever, S. R. Russell, and B. van Ginneken, "Evaluation of a system for automatic detection of diabetic retinopathy from color fundus photographs in a large population of patients with diabetes," *Diabetes Care*, vol. 31, no. 2, pp. 193–198, 2008.

[9] V. Gulshan, L. Peng, M. Coram, et al., "Development and validation of a deep learning algorithm for detection of diabetic retinopathy in retinal fundus photographs," *JAMA*, vol. 316, no. 22, pp. 2402–2410, 2016.

[10] D. S. W. Ting, C. Y.-L. Cheung, G. Lim, et al., "Development and validation of a deep learning system for diabetic retinopathy and related eye diseases using retinal images from multiethnic populations with diabetes," *JAMA*, vol. 318, no. 22, pp. 2211–2223, 2017.

[11] M. D. Abràmoff, P. T. Lavin, M. Birch, N. Shah, and J. C. Folk, "Pivotal trial of an autonomous AI-based diagnostic system for detection of diabetic retinopathy in primary care offices," *npj Digital Medicine*, vol. 1, article 39, 2018.

[12] R. Karthickmanoj, T. Sasilatha, and N. S. S. Singh, "Plant disease detection using random forest classifier with novel segmentation and feature extraction strategy," *Journal of Engineering Science and Technology*, vol. 18, no. 6, pp. 32–38, 2023.

[13] D. P. Yadav, D. Kumar, A. S. Jalal, A. Kumar, K. U. Singh, and M. A. Shah, "Morphological diagnosis of hematologic malignancy using feature fusion-based deep convolutional neural network," *Scientific Reports*, vol. 13, no. 1, article 16988, 2023.

[14] E. Decencière, X. Zhang, G. Cazuguel, et al., "Feedback on a publicly distributed database: the Messidor database," *Image Analysis & Stereology*, vol. 33, no. 3, pp. 231–234, 2014.

[15] T. Kauppi, V. Kalesnykiene, J.-K. Kamarainen, L. Lensu, I. Sorri, A. Raninen, R. Voutilainen, H. Uusitalo, H. Kalviainen, and J. Pietilä, "The DIARETDB1 diabetic retinopathy database and evaluation protocol," in *Proceedings of the British Machine Vision Conference (BMVC)*, 2007, pp. 15.1–15.10.

[16] C. Sinthanayothin, J. F. Boyce, H. L. Cook, and T. H. Williamson, "Automated localisation of the optic disc, fovea, and retinal blood vessels from digital colour fundus images," *British Journal of Ophthalmology*, vol. 83, no. 8, pp. 902–910, 1999.

[17] J. Staal, M. D. Abràmoff, M. Niemeijer, M. A. Viergever, and B. van Ginneken, "Ridge-based vessel segmentation in color images of the retina," *IEEE Transactions on Medical Imaging*, vol. 23, no. 4, pp. 501–509, 2004.

[18] T. Walter, J.-C. Klein, P. Massin, and A. Erginay, "A contribution of image processing to the diagnosis of diabetic retinopathy—Detection of exudates in color fundus images of the human retina," *IEEE Transactions on Medical Imaging*, vol. 21, no. 10, pp. 1236–1243, 2002.

[19] A. Sopharak, B. Uyyanonvara, S. Barman, and T. H. Williamson, "Automatic detection of diabetic retinopathy exudates from non-dilated retinal images using mathematical morphology methods," *Computerized Medical Imaging and Graphics*, vol. 32, pp. 720–727, 2008.

[20] B. Harangi and A. Hajdu, "Automatic exudate detection by fusing multiple active contours and region wise classification," *Computers in Biology and Medicine*, vol. 54, pp. 156–171, 2014.

[21] M. Niemeijer, B. van Ginneken, M. J. Cree, A. Mizutani, et al., "Retinopathy online challenge: automatic detection of microaneurysms in digital color fundus photographs," *IEEE Transactions on Medical Imaging*, vol. 29, no. 1, pp. 185–195, 2010.

[22] H. Attar, A. Solyman, M. A. Deif, M. Hafez, H. M. Kasem, and A.-E. F. Mohamed, "Machine Learning Model Based on Gary-Level Co-occurrence Matrix for Chest Sarcoidosis Diagnosis," in *2023 2nd International Engineering Conference on Electrical, Energy, and Artificial Intelligence (EICEEAI)*, Zarqa, Jordan, 2023, pp. 1–8, doi: 10.1109/EICEEAI60672.2023.10590168.

[23] B. Antal and A. Hajdu, "An ensemble-based system for automatic screening of diabetic retinopathy," *Knowledge-Based Systems*, vol. 60, pp. 20–27, 2014.

[24] H. Pratt, F. Coenen, D. M. Broadbent, S. P. Harding, and Y. Zheng, "Convolutional neural networks for diabetic retinopathy," *Procedia Computer Science*, vol. 90, pp. 200–205, 2016.

[25] R. Gargeya and T. Leng, "Automated identification of diabetic retinopathy using deep learning," *Ophthalmology*, vol. 124, pp. 962–969, 2017.

[26] M. A. Deif, H. Attar, A. Amer, I. A. Elhaty, M. R. Khosravi, and A. A. A. Solyman, "Diagnosis of Oral Squamous Cell Carcinoma Using Deep Neural Networks and Binary Particle Swarm Optimization on Histopathological Images: An AIoMT Approach," *Computational Intelligence and Neuroscience*, vol. 2022, Article ID 6364102, 2022, doi: 10.1155/2022/6364102.

[27] K. Zuiderveld, "Contrast limited adaptive histogram equalization," in *Graphics Gems IV*, P. Heckbert, Ed. San Diego, CA, USA: Academic Press, 1994, pp. 474–485.

[28] A. M. Reza, "Realization of the contrast limited adaptive histogram equalization (CLAHE) for real-time image enhancement," *Journal of VLSI Signal Processing Systems for Signal, Image and Video Technology*, vol. 38, pp. 35–44, 2004.

[29] L. Wang, M. Fei, and T. Yang, "Circular mask and Harris corner detection on rotated images," in *Advanced Computational Methods in Life System Modeling and Simulation*. Springer, 2017, pp. 52–61.

[30] S. Chaudhuri, S. Chatterjee, N. Katz, M. Nelson, and M. Goldbaum, "Detection of blood vessels in retinal images using two-dimensional matched filters," *IEEE Transactions on Medical Imaging*, vol. 8, no. 3, pp. 263–269, 1989.

[31] J. Serra, *Image Analysis and Mathematical Morphology*. London, U.K.: Academic Press, 1982.

[32] R. C. Gonzalez and R. E. Woods, *Digital Image Processing*, 3rd ed. Upper Saddle River, NJ, USA: Prentice Hall, 2008.
[33] N. Otsu, "A threshold selection method from gray-level histograms," *IEEE Transactions on Systems, Man, and Cybernetics*, vol. 9, no. 1, pp. 62–66, 1979.
[34] R. Adams and L. Bischof, "Seeded region growing," *IEEE Transactions on Pattern Analysis and Machine Intelligence*, vol. 16, no. 6, pp. 641–647, 1994.
[35] J. Canny, "A computational approach to edge detection," *IEEE Transactions on Pattern Analysis and Machine Intelligence*, vol. 8, no. 6, pp. 679–698, 1986.
[36] J. Zunić, K. Hirota, and P. L. Rosin, "A Hu invariant as a shape circularity measure," *Pattern Recognition Letters*, vol. 53, pp. 8–13, 2015.
[37] L. Chundan, "1000 Fundus images with 39 categories (JSIEC subset)," Kaggle dataset. Accessed 6 Mar. 2026. Available at: https://www.kaggle.com/datasets/linchundan/fundusimage1000.
[38] openmedlab, "JSIEC dataset summary (Awesome-Medical-Dataset)," GitHub repository page. Accessed 6 Mar. 2026. Available at: https://github.com/openmedlab/Awesome-Medical-Dataset/blob/main/resources/JSIEC.md.
[39] L.-P. Cen, J. Ji, J.-W. Lin, et al., "Automatic detection of 39 fundus diseases and conditions in retinal photographs using deep neural networks," *Nature Communications*, vol. 12, no. 1, pp. 1–13, Aug. 2021, doi: 10.1038/s41467-021-25138-w.
[40] E. R. DeLong, D. M. DeLong, and D. L. Clarke-Pearson, "Comparing the areas under two or more correlated receiver operating characteristic curves: a nonparametric approach," *Biometrics*, vol. 44, no. 3, pp. 837–845, 1988.
[41] M. B. Gonçalves, L. F. Nakayama, D. Ferraz, et al., "Image quality assessment of retinal fundus photographs for diabetic retinopathy in the machine learning era: a review," *Eye*, vol. 38, pp. 426–433, 2024.
[42] K. Zhou, Z. Gu, A. Li, J. Cheng, S. Gao, and J. Liu, "Fundus Image Quality-Guided Diabetic Retinopathy Grading," in *Computational Pathology and Ophthalmic Medical Image Analysis*. Springer, 2018, pp. 245–252.
[43] J. M. Ahn, S. Kim, K.-S. Ahn, S.-H. Cho, K. B. Lee, and U. S. Kim, "A deep learning model for the detection of both advanced and early glaucoma using fundus photography," *PLOS ONE*, vol. 13, no. 11, e0207982, 2018.
[44] P. M. Burlina, N. Joshi, M. Pekala, K. D. Pacheco, D. E. Freund, and N. M. Bressler, "Automated grading of age-related macular degeneration from color fundus images using deep convolutional neural networks," *JAMA Ophthalmology*, vol. 135, no. 11, pp. 1170–1176, 2017.
[45] NHS England, "Diabetic eye screening: Patient grading, referral, surveillance," Guidance updated 25 July 2023.

Haitham Issa received his Ph.D. in Communications and Information systems from Zhejiang University, Hangzhou, China, in 2002. He is currently teaching in the Department of Electrical Engineering in Zarqa University, Zarqa, Jordan. His current research interests include image processing, signal Processing, pattern recognition, machine learning, communication, and renewable energy.

Hani Attar received his Ph.D. from the Department of Electrical and Electronic Engineering, University of Strathclyde, United Kingdom in 2011. Since 2011, he has been working as a researcher of electrical engineering and energy systems. Dr. Attar is now a university lecturer at Zarqa University, Jordan. His research interests include renewable energy systems, efficient designs, and Wireless Communications.

Jafar Ababneh received the B.Sc. degree in telecommunication engineering, in 1991, the M.Sc. degree in 2005, and the Ph.D. degree, in 2009. He is an Associate Professor. In 2009, he joined WISE University as the head of computer information and network systems in information technology (IT) till 2/2022. He was the dean of the IT faculty, WISE University, from August 2015 to November 2020, In 2022, he joined Abdul Aziz Al Ghurair School of Advanced Computing (ASAC), LUMINUS Technical University College (LTUC). He has published many research papers, book chapters, and books in international refereed journals and conferences. His research interests include congestion and network performance, wireless and mobile network, encryption and Information Security, Wireless Sensor Networks (WSNs), Artificial Intelligence, data mining and retrieving information, cloud computing and E-learning.

Zakaria Che Muda is a Professor in Civil Engineering at INTI International University, Malaysia. He received his PhD in Built Environment from the University of Malaya and his MSc in Structural Engineering from the University of Manchester. His research focuses on structural engineering, energy-efficient buildings, and advanced AI applications in engineering.

Ismail A. M. Elhaty is an Assistant Professor in the Department of Nutrition and Dietetics, Faculty of Health Sciences, at Istanbul Gelisim University, Istanbul, Turkey. He earned his bachelor's, master's, and doctoral degrees from United Arab Emirates University. His research interests include plant biochemistry, analytical chemistry, organic chemistry, AI applications in engineering, and environmental pollution.

Ahmed Solyman is a distinguished academic in electrical and electronics engineering, holding a B.Eng. and M.S. from MTC, Egypt, and a Ph.D. from the University of Strathclyde, U.K. With significant contributions to the design of communication and encryption devices. He currently serves as a Lecturer at Glasgow Caledonian University, focusing on wireless communication networks, digital signal processing, IoT, bioinformatics, and AI.

Ramy M. Bahy received the Ph.D. degree in Electrical Engineering from the Military Technical College, Cairo, Egypt, in 2012. His research interests include image and video processing, particularly compression, registration, fusion, and enhancement, with special emphasis on super-resolution techniques. He is also interested in hardware-software interfacing for navigation systems aided by image and video processing, as well as the application of image and video processing in simulators.